EFFICIENT 1-D AND 2-D DOA ESTIMATION FOR NON-CIRCULAR SOURCES WITH HEXAGONAL SHAPED ESPAR ARRAYS

Florian Roemer and Martin Haardt

Ilmenau University of Technology, Communications Research Laboratory
P.O. Box 100565, D-98684 Ilmenau, Germany, http://tu-ilmenau.de/crl
florian.roemer@ieee.org, martin.haardt@tu-ilmenau.de

Abstract — **This contribution is focused on direction of arrival (DoA) estimation with a regular-hexagonal shaped ESPAR (electronically steerable parasitic antenna radiator) array that has received increased attention recently. It is shown how the estimation accuracy is improved by employing non-circular (NC) signal constellations that facilitate the application of the NC Unitary ESPRIT algorithm. It is demonstrated how this method allows the joint estimation of the azimuth and the elevation angles of up to eight uncorrelated sources with a 7-element ESPAR array. Moreover, the achievable benefits of using non-circular sources are assessed by studying deterministic Cramer-Rao bounds. It is shown that for special phase constellations between the impinging wavefronts the estimation accuracy is independent of the angular separation of the corresponding DoAs.**

1. INTRODUCTION

Estimating the directions of arrival of planar wavefronts impinging on an antenna array is a task that has given rise to a manifold of efficient algorithms. It appears in several localization, navigation, and imaging applications and is well known in the context of high resolution parameter estimation from channel sounding measurements.

To facilitate the use of such methods in mobile devices, antenna arrays with low power consumption, small physical size as well as low fabrication cost are required. A recent development promising these features are the so called ESPAR arrays, which have been described in recent publications [1],[2],[4].

To improve the performance of the system even further we propose using non-circular source distributions which facilitate the application of the NC Unitary ESPRIT algorithm [9] that is well known for its high resolution capabilities as well as its low computational complexity and has never been applied to an ESPAR array before. It is very well suited to exploit the invariances of the regular structure of the array as well as the non-circularity of the source distributions. We show that applied to the 7-element ESPAR array, the algorithm is capable of estimating the azimuth and the elevation angle of up to eight sources jointly while automatically enforcing the correct pairing.

This paper is organized as follows. First we introduce our data model and describe the non-circularity condition. Then, the NC Unitary ESPRIT algorithm is briefly summarized. Next, we give a new analytic expression for the deterministic Cramer-Rao bound for non-circular source signals and describe its behavior with respect to the model parameters in a number of lemmas. It is also compared to the Cramer-Rao bound for general signal constellations and the achievable benefit is discussed. Finally, we compare the performance of the algorithm with the Cramer-Rao bound using numerical computer simulations.

The authors gratefully acknowledge the partial support of the German Research Foundation (Deutsche Forschungsgemeinschaft, DFG) under contract no. HA 2239/1-1.

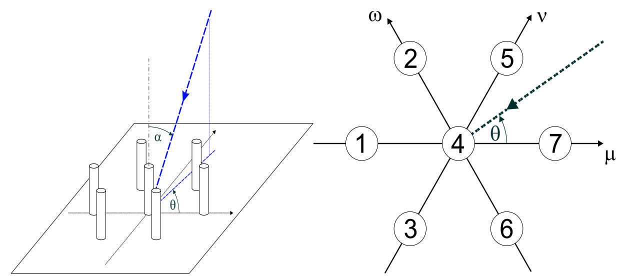

Fig. 1. 7-element ESPAR array configuration. Left: Pseudo-3D-view, showing the azimuth angle θ and the elevation angle α. Right: View from top, showing the three coordinate axes μ, ν, and ω and their relation to the azimuth angle θ as well as how the antenna elements are numbered. Due to hardware restrictions, the distance between adjacent elements is equal to $\lambda/4$ [1].

2. DATA MODEL AND ANTENNA GEOMETRY

Figure 1 shows the configuration of the $M = 7$ sensors in a hexagonal shape. The center element is connected to the single port output of the antenna whereas the other six sensors are positioned at a distance of $\lambda/4$ from the center element (i.e., in its near field) and connected to adjustable varactor diodes. Therefore, the observed scalar output is influenced by the individual sensor outputs, the mutual element coupling and the current reactances of the diodes. By appropriate steering of these reactances it is possible to reconstruct the individual sensor outputs from M sequential scalar measurements, see [2] for details.

In the sequel we assume that this decoupling step has already been performed and we have obtained the M sensor outputs at N subsequent time snapshots from a total of $M \cdot N$ scalar measurements and arranged them in a matrix $\boldsymbol{X} \in \mathbb{C}^{M\times N}$. Assuming that there exist d narrow-band sources in the far-field of the array, we can write $\boldsymbol{X}$ in the following fashion

$$\boldsymbol{X} = \boldsymbol{A} \cdot \boldsymbol{S} + \boldsymbol{N}, \tag{1}$$

where $\boldsymbol{A} \in \mathbb{C}^{M\times d}$ denotes the array steering matrix which consists of d array steering vectors $\boldsymbol{a}_1, \ldots, \boldsymbol{a}_d$, $\boldsymbol{S} \in \mathbb{C}^{d\times N}$ contains N subsequent symbols from the d users, and $\boldsymbol{N} \in \mathbb{C}^{M\times N}$ represents samples of the additive noise component which are assumed to be Gaussian distributed and mutually uncorrelated. Further insight into the structure of $\boldsymbol{S}$ for non-circular signals is given in Chapter 3.

In order to fully exploit the regular geometry of the array, let us consider three spatial frequencies μ, ν, and ω as described in [8]. Their axes correspond to the symmetry axes of the hexagonal structure. Then, the array steering vector can be written as

$$\boldsymbol{a}\left(\mu,\nu,\omega\right)=\left[e^{-j\mu},e^{j\omega},e^{-j\nu},1,e^{j\nu},e^{-j\omega},e^{j\mu}\right]^{T},\quad(2)$$

following the numbering of the sensors we have defined in Figure 1. Notice, that

$$\boldsymbol{\Pi}\cdot\boldsymbol{a}^{*}=\boldsymbol{a},\ \text{and hence}\ \boldsymbol{\Pi}\cdot\boldsymbol{A}^{*}=\boldsymbol{A}\quad(3)$$

where $\boldsymbol{\Pi}$ represents the exchange matrix having ones on its antidiagonal and zeros elsewhere and the asterisk denotes complex conjugation. In other words, the phase center of the array is chosen such that the array steering matrix is left-$\boldsymbol{\Pi}$-real.

The spatial frequencies depend on the direction of arrival angles in the following fashion

$$\begin{aligned}\mu(\theta,\alpha)&=\pi/2\cdot\cos\left(\theta\right)\cdot\sin\alpha &(4)\\ \nu(\theta,\alpha)&=\pi/2\cdot\cos\left(\theta-60^{\circ}\right)\cdot\sin\alpha &(5)\\ \omega(\theta,\alpha)&=\pi/2\cdot\cos\left(\theta-120^{\circ}\right)\cdot\sin\alpha, &(6)\end{aligned}$$

where θ represents the azimuth and α the elevation angle, which should be set to 90° in the 1-D case. Figure 1 also illustrates how the angles are defined. Inserting these equations into equation (2) yields the array steering vectors in terms of the direction of arrival angles.

The spatial frequencies are chosen such that the array is shift invariant along all the three directions we defined. Thus, we can establish shift invariance equations for each of the spatial frequencies individually. In each case $m=4$ out of the $M=7$ elements belong to one subarray. The corresponding selection matrices $\boldsymbol{J}_{\mu,1}$, $\boldsymbol{J}_{\mu,2}$, $\boldsymbol{J}_{\nu,1}$, $\boldsymbol{J}_{\nu,2}$, $\boldsymbol{J}_{\omega,1}$, and $\boldsymbol{J}_{\omega,2}$ are defined in [8].

3. NON-CIRCULAR SIGNALS

NC Unitary ESPRIT relies on the fact that the source waveforms are non-circular, i.e., viewed in the complex I-Q-diagram, the amplitudes lie on one line for each user. This condition imposes further restrictions on the symbol matrix. Since only non-circular signals are allowed, each row in $\boldsymbol{S}$ needs to be real-valued except for a complex scaling term. Thus, we can write $\boldsymbol{S}$ in the following form

$$\boldsymbol{S}=\boldsymbol{\Psi}\cdot\boldsymbol{S}_{0},\quad(7)$$

where $\boldsymbol{S}_0\in\mathbb{R}^{M\times d}$ and $\boldsymbol{\Psi}=\operatorname{diag}\left\{e^{j\varphi_i}\right\}_{i=1}^{d}$ contains the arbitrary phase shifts that can be different for each user. Such a scenario is, for example, found when the users transmit real-valued data but have different transmit delays which determine the matrix $\boldsymbol{\Psi}$.

Under these conditions it has been shown in [9] that we can extend the measurement matrix in the following way

$$\boldsymbol{X}^{(\mathrm{nc})}=\left[\begin{array}{c}\boldsymbol{X}\\ \boldsymbol{\Pi}_{M}\boldsymbol{X}^{*}\end{array}\right]\in\mathbb{C}^{2M\times N}.\quad(8)$$

Using our new data model from equations (1), (3), and (7) we obtain the following factorization

$$\begin{aligned}\boldsymbol{X}^{(\mathrm{nc})}&=\boldsymbol{A}^{(\mathrm{nc})}\cdot\boldsymbol{S}+\boldsymbol{N}^{(\mathrm{nc})},\ \text{where} &(9)\\ \boldsymbol{A}^{(\mathrm{nc})}&=\left[\begin{array}{c}\boldsymbol{A}\\ \boldsymbol{A}\,\boldsymbol{\Psi}^{*}\,\boldsymbol{\Psi}^{*}\end{array}\right],\ \text{and}\ \boldsymbol{N}^{(\mathrm{nc})}=\left[\begin{array}{c}\boldsymbol{N}\\ \boldsymbol{\Pi}\,\boldsymbol{N}^{*}\end{array}\right],\end{aligned}$$

which is similar to (1).

Since the new array steering matrix $\boldsymbol{A}^{(\mathrm{nc})}$ is of size $2M\times d$, we have virtually doubled the number of antennas, which yields a better resolution and a higher number of separable sources. Moreover, it can easily be shown that (8) includes the forward-backward-averaging preprocessing step needed for Unitary ESPRIT [3].

4. 3-D NC UNITARY ESPRIT

In order to estimate the spatial frequencies along the three coordinate axes jointly, we combine the NC Unitary ESPRIT algorithm [9] with Unitary ESPRIT for ESPAR arrays [8]. In this chapter we just summarize the main steps of this combined estimation procedure.

(1) Signal subspace estimation The signal subspace matrix will be called $\boldsymbol{E}_s\in\mathbb{R}^{2M\times d}$ and it can be obtained by a real-valued SVD of

$$\boldsymbol{\varphi}(\boldsymbol{X})=\left[\begin{array}{cc}\operatorname{Re}\{\boldsymbol{X}\}^{T} & \operatorname{Im}\{\boldsymbol{X}\}^{T}\end{array}\right]^{T}.\quad(10)$$

(2) Solution of the shift invariance equations Once the signal subspace has been estimated we can establish the shift invariance equations for the three spatial frequencies

$$\begin{aligned}\boldsymbol{K}_{\mu,1}^{(\mathrm{nc})}\cdot\boldsymbol{E}_s\cdot\boldsymbol{\Upsilon}_{\mu}&\approx\boldsymbol{K}_{\mu,2}^{(\mathrm{nc})}\cdot\boldsymbol{E}_s &(11)\\ \boldsymbol{K}_{\nu,1}^{(\mathrm{nc})}\cdot\boldsymbol{E}_s\cdot\boldsymbol{\Upsilon}_{\nu}&\approx\boldsymbol{K}_{\nu,2}^{(\mathrm{nc})}\cdot\boldsymbol{E}_s &(12)\\ \boldsymbol{K}_{\omega,1}^{(\mathrm{nc})}\cdot\boldsymbol{E}_s\cdot\boldsymbol{\Upsilon}_{\omega}&\approx\boldsymbol{K}_{\omega,2}^{(\mathrm{nc})}\cdot\boldsymbol{E}_s, &(13)\end{aligned}$$

which represent three overdetermined sets of equations that need to be solved for the $\boldsymbol{\Upsilon}$-matrices. Here, the matrices $\boldsymbol{K}_{\eta,i}^{(\mathrm{nc})},\ \eta\in\{\mu,\nu,\omega\},i=1,2$ are obtained from the selection matrices $\boldsymbol{J}_{\eta,i}$ by using the transformation

$$\begin{aligned}\boldsymbol{K}_{\eta,1}^{(\mathrm{nc})}&=2\cdot\operatorname{Re}\{\boldsymbol{Q}_{2m}^{H}\boldsymbol{J}_{\eta,2}^{(\mathrm{nc})}\boldsymbol{Q}_{2M}\}\ \in\mathbb{R}^{2m\times 2M} &(14)\\ \boldsymbol{K}_{\eta,2}^{(\mathrm{nc})}&=2\cdot\operatorname{Im}\{\boldsymbol{Q}_{2m}^{H}\boldsymbol{J}_{\eta,2}^{(\mathrm{nc})}\boldsymbol{Q}_{2M}\}\ \in\mathbb{R}^{2m\times 2M}, &(15)\\ \boldsymbol{J}_{\eta,i}^{(\mathrm{nc})}&=\boldsymbol{I}_2\otimes\boldsymbol{J}_{\eta,i} &(16)\end{aligned}$$

where the $\boldsymbol{Q}_p$ are unitary left-$\boldsymbol{\Pi}$-real matrices, $\boldsymbol{I}_2$ represents the identity matrix of size 2×2, and $\otimes$ the Kronecker product operator.

(3) Joint diagonalization In order to achieve automatic pairing of the spatial frequencies after solving equations (11), (12), and (13) for the $\boldsymbol{\Upsilon}$-matrices, we need to compute their eigenvalues jointly, i.e., we need to determine matrices $\boldsymbol{U}_{\mu}$, $\boldsymbol{U}_{\nu}$, and $\boldsymbol{U}_{\omega}$, such that

$$\begin{aligned}\boldsymbol{U}_{\mu}&=\boldsymbol{\Theta}^{T}\,\boldsymbol{\Upsilon}_{\mu}\,\boldsymbol{\Theta} &(17)\\ \boldsymbol{U}_{\nu}&=\boldsymbol{\Theta}^{T}\,\boldsymbol{\Upsilon}_{\nu}\,\boldsymbol{\Theta} &(18)\\ \boldsymbol{U}_{\omega}&=\boldsymbol{\Theta}^{T}\,\boldsymbol{\Upsilon}_{\omega}\,\boldsymbol{\Theta}, &(19)\end{aligned}$$

$\boldsymbol{\Theta}$ is a real-valued unitary matrix, and $\boldsymbol{U}_{\mu}$, $\boldsymbol{U}_{\nu}$, $\boldsymbol{U}_{\omega}$ are as upper triangular as possible in a least squares sense. This task can be accomplished by a simultaneous Schur decomposition, a joint diagonalization technique discussed in detail in [5].

(4) Spatial frequencies Using the matrices $\boldsymbol{U}_{\mu}$, $\boldsymbol{U}_{\nu}$, and $\boldsymbol{U}_{\omega}$ from (17), (18), and (19), the estimates for the spatial frequencies are obtained from their diagonal elements

$$\left.\begin{array}{l}\hat{\mu}_i=2\cdot\arctan\left(\left[\boldsymbol{U}_{\mu}\right]_{i,i}\right)\\ \hat{\nu}_i=2\cdot\arctan\left(\left[\boldsymbol{U}_{\nu}\right]_{i,i}\right)\\ \hat{\omega}_i=2\cdot\arctan\left(\left[\boldsymbol{U}_{\omega}\right]_{i,i}\right)\end{array}\right\}\quad i=1,2,\ldots,d.$$

(5) 1-D and 2-D DoA angles Once we have calculated estimates for the spatial frequencies, there are various ways to obtain estimates for the direction of arrival angles from them. These approaches are discussed and compared in detail in [8] and will not be repeated here since they apply to Unitary ESPRIT in the same way as they apply to NC Unitary ESPRIT. For the simulations in this work, least squares combining is used. For each source, the azimuth and elevation angles are computed by solving [8]

$$\begin{aligned} \tan\hat{\theta} &= \frac{\sqrt{3}(\hat{\nu}+\hat{\omega})}{2\hat{\mu}+\hat{\nu}-\hat{\omega}} \\ \sin\hat{\alpha} &= \frac{4}{3\pi}\sqrt{\hat{\mu}^2+\hat{\nu}^2+\hat{\omega}^2+\hat{\mu}\hat{\nu}+\hat{\nu}\hat{\omega}-\hat{\mu}\hat{\omega}} \end{aligned}$$

5. PERFORMANCE

In this chapter we study the Cramer-Rao bound for our non-circular data model and compare it to the Cramer-Rao bound for general source signals. Here we only consider deterministic Cramer-Rao bounds and we assume that the average symbol energy is equal to P for all users. Note that the results do not coincide with [7], because non-circularity was defined in another way there.

Lemma 1

The DoA-related block of the deterministic Cramer-Rao bound for our new data model is given by

$$\begin{aligned} \boldsymbol{C}^{(\mathrm{nc})} &= \frac{\sigma^2}{N}\cdot\left(\left[\boldsymbol{D}^{(\mathrm{nc})^H}\cdot\boldsymbol{\Pi}^{\perp}_{A^{(\mathrm{nc})}}\cdot\boldsymbol{D}^{(\mathrm{nc})}\right]\odot\hat{\boldsymbol{R}}_S\right)^{-1}, \text{where} \\ \boldsymbol{\Pi}^{\perp}_{A^{(\mathrm{nc})}} &= \boldsymbol{I}_{14}-\boldsymbol{A}^{(\mathrm{nc})}\left(\boldsymbol{A}^{(\mathrm{nc})^H}\boldsymbol{A}^{(\mathrm{nc})}\right)^{-1}\boldsymbol{A}^{(\mathrm{nc})^H}, \\ \boldsymbol{D}^{(\mathrm{nc})} &= \begin{bmatrix}\boldsymbol{D}\\ \boldsymbol{D}\,\boldsymbol{\Psi}^*\,\boldsymbol{\Psi}^*\end{bmatrix},\ \boldsymbol{D}=\left[\frac{\partial\boldsymbol{a}_1}{\partial\theta_1},\ldots,\frac{\partial\boldsymbol{a}_d}{\partial\theta_d}\right], \\ \hat{\boldsymbol{R}}_S &\doteq \frac{1}{N}\boldsymbol{S}\boldsymbol{S}^H=\boldsymbol{\Psi}\hat{\boldsymbol{R}}_{S0}\boldsymbol{\Psi}^*,\ \text{and}\ \hat{\boldsymbol{R}}_{S0}\doteq\frac{1}{N}\boldsymbol{S}_0\boldsymbol{S}_0^H. \end{aligned}$$

This CRB can be compared with the classic CRB for the deterministic case (see, e.g., [6])

$$\begin{aligned} \boldsymbol{C} &= \frac{\sigma^2}{2N}\cdot\left(\left[\boldsymbol{D}^H\cdot\boldsymbol{\Pi}^{\perp}_A\cdot\boldsymbol{D}\right]\odot\hat{\boldsymbol{R}}_S\right)^{-1}, \text{where} \\ \boldsymbol{\Pi}^{\perp}_A &= \boldsymbol{I}_7-\boldsymbol{A}\left(\boldsymbol{A}^H\boldsymbol{A}\right)^{-1}\boldsymbol{A}^H. \end{aligned}$$

Notice, that $\boldsymbol{C}^{(\mathrm{nc})}$ has the same form as $\boldsymbol{C}$ except for a factor of 2 and the array matrices $\boldsymbol{A}$ and $\boldsymbol{D}$ being replaced by the modified array matrices $\boldsymbol{A}^{(\mathrm{nc})}$ and $\boldsymbol{D}^{(\mathrm{nc})}$, respectively.

Lemma 2

For a single-source estimation problem (i.e., $d=1$), the CRB's are given by

$$\boldsymbol{C}=\boldsymbol{C}^{(\mathrm{nc})}=\frac{2}{3\pi^2}\cdot\frac{\sigma^2}{P\cdot N}, \tag{20}$$

i.e., they are independent of the direction of arrival angle θ as well as the scalar parameter Ψ. Consequently, the ESPAR array is capable of providing the same estimation accuracy for every possible direction. Moreover, there is no gain from using non-circular signals if there is only one source.

Lemma 3

The modified CRB depends strongly on $\boldsymbol{\Psi}$. In particular, for the case where $\boldsymbol{\Psi}=\boldsymbol{I}$, we have

$$\boldsymbol{C}=\boldsymbol{C}^{(\mathrm{nc})}\doteq\boldsymbol{C}_0, \tag{21}$$

and for any $\boldsymbol{\Psi}\neq\boldsymbol{I}$, the CRB is smaller than $\boldsymbol{C}_0$. In other words, $\boldsymbol{\Psi}=\boldsymbol{I}$ corresponds to the worst case for all possible $\boldsymbol{\Psi}$.

Lemma 4

For $d=2$ users, a phase separation $\Delta\varphi\doteq\varphi_1-\varphi_2$ of $\pm\pi/2+k\pi$ yields the following CRB

$$\boldsymbol{C}^{(\mathrm{nc})}=\frac{2}{3\pi^2}\cdot\frac{\sigma^2}{P\cdot N}\cdot\boldsymbol{I}_2. \tag{22}$$

As we can see for this particular $\boldsymbol{\Psi}$, the CRB is completely independent of the direction of arrival angles and the correlation between the two sources. In other words, regardless of how closely they are spaced, the CRB for both of the users is the same as the CRB in the single user case, which is a very significant benefit compared to the solution for general source constellations.

It can also be shown that for two users $\boldsymbol{C}^{(\mathrm{nc})}(\Delta\varphi)$ is symmetric in $\Delta\varphi$ and π-periodic. Consequently, only the interval $\Delta\varphi\in[0,\pi/2]$ has to be considered. Moreover, it is easy to prove that in this interval $\boldsymbol{C}^{(\mathrm{nc})}(\Delta\varphi)$ decreases monotonically. Therefore, $\Delta\varphi=0$ corresponds to the worst case and $\Delta\varphi=\pm\pi/2+k\cdot\pi$ to the best case. The gap between these two cases increases with decreasing source separation.

Note that for uncorrelated sources, $\boldsymbol{C}$ is independent of $\Delta\varphi$ (but still dependent on $\Delta\theta$), whereas for coherent sources it also decreases monotonically as $\Delta\varphi$ goes from 0 to $\pi/2$.

Lemma 5

Lemma 4 can be generalized to d sources: If there are only two different phases in $\boldsymbol{\Psi}$, i.e., φ_i is either equal to φ_1 or φ_2 for all $i=1,2,\ldots,d$ then in the case where $\Delta\varphi=|\varphi_1-\varphi_2|=\pi/2$ the users with phase φ_1 are completely decoupled from the users with phase φ_2. The Fisher information matrix as well as the CRB matrix become block diagonal (after appropriate reordering) with two blocks corresponding to the two groups of users.

While the conditions for this lemma seem rather restrictive it may have significant practical relevance in a system, where the matrix $\boldsymbol{\Psi}$ can be influenced on purpose. Whether or not we have control over it depends on the system. [1]

Now assume that we have perfect control over the phases and that we are able to estimate them without error. Then, one possible (though not necessarily the best) choice for $\boldsymbol{\Psi}$ can be constructed from Lemma 5. One may divide the users into two groups and assign the delays such that the groups decouple as described by the lemma. The remaining task would then be to assign the users to groups in such a way that users with small angular separation belong to different groups, which is easily achieved.

Lemma 6

The CRB's can be generalized to the 2-D DoA estimation case. Here we have $2d$ direction of arrival parameters: $\theta_i,\alpha_i,\ i=1,2,\ldots,d$. Hence, the DoA-related blocks of the CRB matrices are now of size $2d\times 2d$. They can be calculated in the following fashion

$$\begin{aligned} \boldsymbol{C}^{(\mathrm{nc})} &= \frac{\sigma^2}{N}\cdot\left(\left[\boldsymbol{D}_{2D}^{(\mathrm{nc})^H}\cdot\boldsymbol{\Pi}^{\perp}_{A^{(\mathrm{nc})}}\cdot\boldsymbol{D}_{2D}^{(\mathrm{nc})}\right]\odot(\boldsymbol{I}_2\otimes\hat{\boldsymbol{R}}_S)\right)^{-1} \\ \boldsymbol{C} &= \frac{\sigma^2}{2N}\cdot\left(\left[\boldsymbol{D}_{2D}^H\cdot\boldsymbol{\Pi}^{\perp}_A\cdot\boldsymbol{D}_{2D}\right]\odot\hat{\boldsymbol{R}}_S\right)^{-1},\quad \text{where} \\ \boldsymbol{D}_{2D} &= \left[\frac{\partial\boldsymbol{a}_1}{\partial\theta_1},\ldots,\frac{\partial\boldsymbol{a}_d}{\partial\theta_d},\frac{\partial\boldsymbol{a}_1}{\partial\alpha_1},\ldots,\frac{\partial\boldsymbol{a}_d}{\partial\alpha_d}\right],\quad \text{and} \\ \boldsymbol{D}_{2D}^{(\mathrm{nc})} &= \left[\frac{\partial\boldsymbol{a}_1^{(\mathrm{nc})}}{\partial\theta_1},\ldots,\frac{\partial\boldsymbol{a}_d^{(\mathrm{nc})}}{\partial\theta_d},\frac{\partial\boldsymbol{a}_1^{(\mathrm{nc})}}{\partial\alpha_1},\ldots,\frac{\partial\boldsymbol{a}_d^{(\mathrm{nc})}}{\partial\alpha_d}\right]. \end{aligned}$$

[1] In a communications system controlling $\boldsymbol{\Psi}$ would require the base station to estimate the phases and to transmit feedback information to the users. Since $\boldsymbol{\Psi}$ arises from propagation delays it can be altered by delaying the users' transmissions by an appropriate fraction of one carrier period.

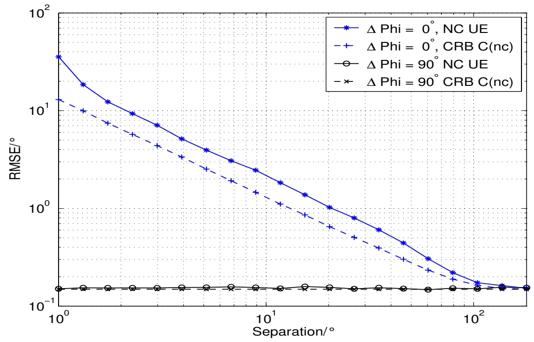

Fig. 2. RMSE of NC Unitary ESPRIT versus the angular separation $\Delta\theta$ of $d = 2$ uncorrelated users for two different phase separations. The dashed lines represent the corresponding CRBs.

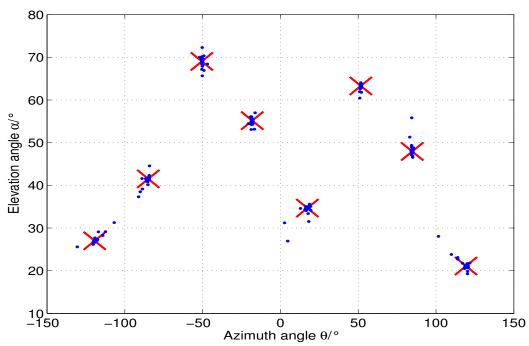

Fig. 3. Scatter plot demonstrating that NC Unitary ESPRIT is able to estimate azimuth and elevation of up to 8 sources jointly with correct pairing. The SNR is 40 dB, $N = 10000$ snapshots are used.

6. SIMULATION RESULTS

In this chapter numerical computer simulations are presented to demonstrate the capabilities of the NC Unitary ESPRIT algorithm and to compare it with the Cramer-Rao bounds discussed in the previous chapter. For all of the following simulations, a BPSK modulation scheme is assumed. Different users are assumed to be mutually uncorrelated. If not stated otherwise, the number of snapshots N is set to 20, and an SNR of 30 dB is used.

Figure 2 illustrates the performance of the algorithm for closely spaced sources located at 42° and $42^\circ + \Delta\theta$, respectively. The phase separation $\Delta\varphi$ is set to $\pi/2$ for the top curve and 0 for the bottom curve. The dashed lines represent the corresponding CRB's. We can clearly see how the estimation error becomes independent of the source separation for the best case of $\Delta\varphi = \pi/2$. Thus for small angular separations the gap between the best and the worst case phase separation becomes very large.

The next simulation result shows the algorithms' ability to jointly estimate azimuth and elevation of up to 8 sources. For this simulation $N = 10000$ snapshots are used and the SNR is equal to 40 dB. The red crosses in Figure 3 indicate the correct location of the users and the blue dots represent estimates of 500 independent simulation runs.

Finally, in Figure 4 we compare the RMSE of Unitary ESPRIT and NC Unitary ESPRIT along with the corresponding CRB's. The optimal $\Delta\varphi$ of $\pi/2$ is used and the sources are positioned at 30° and 37°. We can see that the use of NC Unitary ESPRIT is beneficial since the estimation errors are significantly smaller.

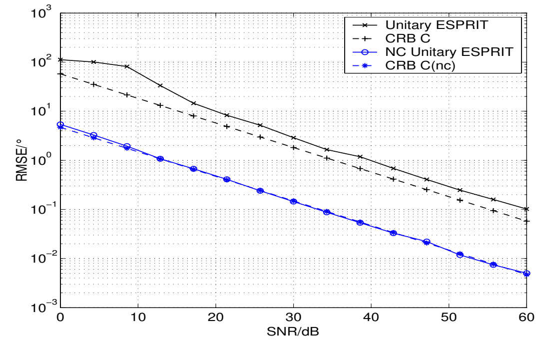

Fig. 4. Comparison between Unitary ESPRIT and NC Unitary ESPRIT with their corresponding CRBs. Here, the $d = 2$ sources are positioned at 30° and 37° and $\Delta\varphi$ is set to $\pi/2$.

7. CONCLUSIONS

In this paper we study the estimation of direction of arrival angles with a 7-element ESPAR array using non-circular source signals. For this configuration we derive new explicit expressions for the CRB's in the 1-D and the 2-D cases. Some important special cases are discussed. In particular, for a single source the CRB is always independent of the azimuth angle and for two sources it becomes independent of both azimuth angles if the phase separation $\Delta\varphi$ is $\pm\pi/2 + k \cdot \pi$.

We also describe the operation of the NC Unitary ESPRIT algorithm which is capable of estimating 1-D and 2-D direction of arrival angles of up to eight sources with automatic pairing. The performance of the algorithm is close to the CRB.

Note that the algorithms and bounds we present in this paper can be extended in a straightforward fashion to larger hexagonal arrays with $M = 3n^2 + 3n + 1, n \in \mathbb{N}$ sensors. These arrays are constructed by putting more slices of sensors around the inner hexagon as shown in [8].

8. REFERENCES

[1] E. Taillefer, E. Chu, and T. Ohira, "ESPRIT Algorithm for a Seven-Element Regular-Hexagonal Shaped ESPAR Antenna", *Proc. European Conference on Wireless Technology (ECWT 2004),* Amsterdam, The Netherlands, Oct. 2004.

[2] S. Chandran, *Adaptive Antenna Arrays: Trends and Applications,* Springer-Verlag, 2004, ch. Analog Smart Antennas, ISBN 3-540-20199-8.

[3] M. Haardt, *Efficient One-, Two-, and Multidimensional High-Resolution Array Signal Processing*, Shaker Verlag, Aachen, Germany, 1996, ISBN 3-8265-2220-6.

[4] C. Plapous, J. Cheng, E. Taillefer, A. Hirata, and T. Ohira, "Reactance domain MUSIC algorithm for ESPAR antennas", in 33^{rd} *European Microwave Conference EuMW2003,* Munich Oct. 2003, pp. 793-796.

[5] M. Haardt and J. A. Nossek, "Simultaneous Schur decomposition of several non-symmetric matrices to achieve automatic pairing in multidimensional harmonic retrieval problems", *IEEE Trans. Signal Processing,* vol. 46, pp. 161-169, Jan. 1998.

[6] P. Stoica and A. Nehorai, "Music, Maximum Likelihood and the Cramer-Rao bound", *IEEE Transaction on Acoustics, Speech and Signal Processing,* vol. 37, no. 5, pp. 720-741, May 1989.

[7] J.-P. Delmas and H. Abeida, "Stochastic CRB for Noncircular Signals with Application to DOA Estimation", *IEEE Transactions on Signal Processing,* vol. 52, no. 11, pp. 3192-3199, Nov 2004.

[8] F. Roemer and M. Haardt, "Using 3-D Unitary ESPRIT on a Hexagonal Shaped ESPAR Antenna for 1-D and 2-D DOA Estimation", in *IEEE/ITG Workshop on Smart Antennas,* Duisburg, Germany, Apr 2005.

[9] M. Haardt and F. Roemer, "Enhancements of Unitary ESPRIT for non-circular sources", *Proc. International Conference on Acoustics, Speech and Signal Processing (ICASSP 2004),* Montreal, Canada, May 2004.